

ARTICLE

Open Access

Zero-power infrared switch with two-phase microfluidic flow and a 2D material thermal isolation layer

Zekun Zhang¹, Peng Li²✉ and Yixuan Zou¹

Abstract

Wireless sensor nodes (WSNs) play an important role in many fields, including environmental monitoring. However, unattended WSNs face challenges in consuming power continuously even in the absence of useful information, which makes energy supply the bottleneck of WSNs. Here, we realized zero-power infrared switches, which consist of a metasurface and two-phase microfluidic flow. The metasurface can recognize the infrared signal from the target and convert it into heat, which triggers the two-phase microfluidic flow switch. As the target is not present, the switch is turned off. The graphene/MoS₂/graphene 2D material heterostructure (thickness <2 nm) demonstrates an exceptionally high thermal resistance of 4.2 K/W due to strong phonon scattering and reduces the heat flow from the metasurface to the supporting substrate, significantly increasing the device sensitivity (the displacement of the two-phase microfluidic flow increases from ~1500 to ~3000 μm). The infrared switch with a pair of symmetric two-phase microfluidic flows can avoid spurious triggering resulting from environmental temperature changes. We realized WSNs with near-zero standby power consumption by integrating the infrared switch, sensors, and wireless communication module. When the target infrared signal appears, the WSNs are woken and show superb visual/auditory sensing performance. This work provides a novel approach for greatly lengthening the lifespan of unattended WSNs.

Introduction

With the development of the Internet of Things (IoT), a multitude of wireless sensor nodes (WSNs) have been deployed, which play crucial roles in industrial automation, environmental monitoring, and many other fields^{1–4}. However, the application of unattended WSNs is currently constrained by the energy supply⁵. In scenarios such as forest fires or gas leaks^{6,7}, which are infrequent but critical, traditional WSNs powered by batteries face challenges of continuous power consumption even in the absence of useful information^{8,9}. Frequently charging or replacing batteries largely reduces the significance of unattended WSNs.

The integration of WSNs with triboelectric or piezoelectric nanogenerators presents a promising avenue for prolonging the lifespan of sensor nodes through the provision of supplementary power sources^{10–14}. Nevertheless, the electrical power derived from the current energy harvesting technique tends to be limited and unstable, which makes ensuring the timely functioning of WSNs challenging. Another method of extending the lifespan of sensor nodes is the deployment strategy along with algorithmic adjustments, which can effectively reduce the overall power consumption of large-scale WSN networks^{15,16}, but they are unable to completely eliminate substantial standby power consumption.

Employing devices that harness the signal/energy from the target to awake sensor nodes is a promising strategy that can largely reduce energy consumption in standby mode^{8,17,18}. However, an electrical circuit is needed to derive the wake-up signal. Although low-power electrical circuits can be used, standby power consumption

Correspondence: Peng Li (lipeng2023@hust.edu.cn)

¹Department of Precision Instruments, Tsinghua University, 100084 Beijing, China

²School of Mechanical Science and Engineering, Huazhong University of Science and Technology, 430074 Wuhan, China

© The Author(s) 2024



Open Access This article is licensed under a Creative Commons Attribution 4.0 International License, which permits use, sharing, adaptation, distribution and reproduction in any medium or format, as long as you give appropriate credit to the original author(s) and the source, provide a link to the Creative Commons licence, and indicate if changes were made. The images or other third party material in this article are included in the article's Creative Commons licence, unless indicated otherwise in a credit line to the material. If material is not included in the article's Creative Commons licence and your intended use is not permitted by statutory regulation or exceeds the permitted use, you will need to obtain permission directly from the copyright holder. To view a copy of this licence, visit <http://creativecommons.org/licenses/by/4.0/>.

cannot be avoided. Therefore, devices that can generate wake-up signals without the need for electrical circuits are highly desirable. Truong et al. fabricated a MEMS (microelectromechanical system) switch with a 5 nm gap between the microcantilever and the substrate¹⁹. As target gas molecules were captured by the molecular chains decorated on the microcantilever and substrate surfaces, the switch was turned on. However, the extremely small gap (5 nm) between the microcantilever and substrate poses challenges to device manufacturing and stability. Qian et al. developed a near-zero-standby-power infrared switch by employing a metasurface to convert infrared energy into heat and actuated a microcantilever beam to bend and connect the metal pad²⁰. Since the infrared energy emitted from the target is extremely low, elongated microcantilever beams and extremely small gaps are needed. As such, device fabrication is extremely challenging and has the problem of easy spurious triggering by vibration and electrostatic attraction. Moreover, the device lacked self-holding ability, indicating that it rapidly turned off once the target infrared radiation disappeared, which did not provide sufficient time for WSNs to complete data acquisition and processing. Therefore, there is an urgent need for easily fabricated, reliable, zero-standby-power WSNs with self-holding ability.

In this work, we developed an easily fabricated, reliable, zero-power infrared switch by integrating a metasurface (MS), two-phase microfluidic flow, and a 2D material heterostructure thermal isolation layer. The metasurface can recognize the infrared signals emitted from the target and convert them into heat, which turns on the two-phase microfluidic flow switch. The two-phase microfluidic flow switch is slowly turned off as the target infrared signal disappears, demonstrating self-holding ability. On the basis of this technique, we realized near-zero standby power WSNs.

Experiment

Fabrication of the MS with a 2D material thermal isolation layer

The MS has a metal-insulator-metal (MIM) sandwich structure on a graphene/MoS₂/graphene heterostructure. Chemical vapor deposition (CVD)-grown monolayer graphene/MoS₂/graphene was transferred onto a 200 μm-thick glass substrate as a thermal isolation layer. Then, 5 nm Cr/40 nm Au/5 nm Cr (reflection layer) was deposited on the thermal isolation layer and patterned via photolithography, electron-beam evaporation, and a metal lift-off process. A 300-nm-thick silicon nitride film (dielectric layer) was subsequently deposited via plasma-enhanced chemical vapor deposition (PECVD) on the reflection layer. The metal arrays were fabricated on top of the dielectric

layer via electron-beam lithography, evaporation, and metal lift-off.

Fabrication of the two-phase microfluidic switch

A glass substrate with a liquid reservoir and microchannel (channel width <40 μm) was fabricated with a laser cutting machine. The electrodes on the glass substrate were derived via photolithography, electron-beam evaporation, and metal lift-off. The MA was placed into the reservoir. Then, the glasses were bonded together with a UV-curable adhesive. The liquid reservoir and part of the microchannel were filled with kerosene as an insulating liquid via the vacuum-assisted method. A trace amount of conductive FeCl₃ solution (~0.1 nL) was filled into the microchannel and formed a two-phase microfluidic flow with kerosene.

Device measurements

We employed a 170-mW blackbody light source, CaF₂ glasses, ZnS lenses, and various filters to generate infrared light with different wavelengths and irradiate the infrared switch. A digital multimeter (Keysight 34470) was used to measure the resistance/current of the two-phase microfluidic switch in the infrared switch. A digital power meter was used to measure the power consumption of the unattended WSNs.

Results and discussion

Device structure and working mechanism

As shown in Fig. 1a, b, the infrared switch consists of two two-phase microfluidic switches. Each two-phase microfluidic switch comprises a microchannel with electrode arrays and a reservoir. The reservoir and part of the channel are filled with kerosene. Kerosene is chosen because it is transparent to infrared signals. Insulating kerosene and conductive FeCl₃ solution (two immiscible solutions) form a two-phase microfluidic flow in the microchannel. The MS with a 2D material thermal isolation layer is placed in the reservoir and completely immersed in kerosene (only 1 microfluidic switch is integrated with the MS). The infrared signal passes through an infrared-transparent CaF₂ glass and kerosene and irradiates the MS, which converts the infrared signal into heat. The heat results in kerosene expansion in the liquid reservoir, thereby pushing the trace FeCl₃ solution forward in the microchannel. When the infrared energy absorbed by the MS surpasses a certain value, the trace FeCl₃ solution is connected to the proper pair of metal electrodes, and the switch is turned on, as shown in Fig. 1d. Under ambient temperature variation, the FeCl₃ solutions in both microchannels move simultaneously without activating the infrared switch, indicating that spurious triggering resulting from environmental temperature changes can be avoided.

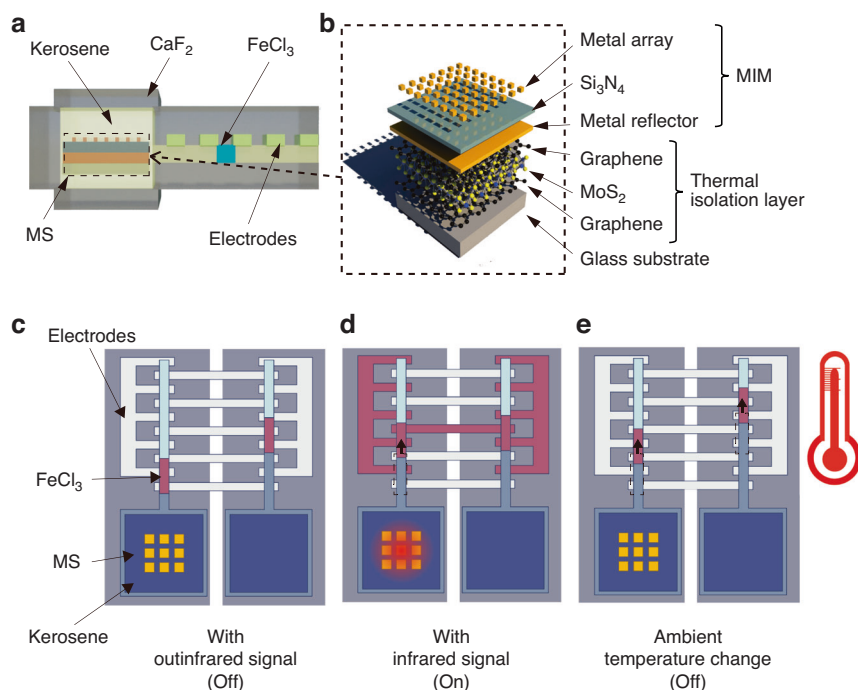


Fig. 1 Infrared switch. **a** Cross-sectional view of the infrared switch with the MS and a two-phase microfluidic switch. **b** Schematic view of the MS with a graphene/MoS₂/graphene 2D material heterostructure thermal isolation layer. **c** Infrared switch in the 'off' state without a target infrared signal (top view). **d** Infrared switch in the 'on' state with a target infrared signal. **e** The infrared switch can avoid spurious triggering resulting from environmental temperature changes

Metasurface

The MS can recognize the infrared signals emitted from the target and convert the signals into heat. Compared with traditional infrared absorbing materials, the MS is much smaller in size and has better absorptivity. It also has excellent wavelength selectivity^{21–24}. The MS has a metal-insulator-metal (MIM) sandwich structure. The transmittance of the MS is negligible owing to the reflection layer. The geometrical sizes of the top metal arrays are crucial for the absorptivity and absorption wavelength. The impedance of the MS should match the free space impedance:

$$Z_0 = \sqrt{\mu(\omega)/\epsilon(\omega)} \quad (1)$$

where Z_0 is the characteristic impedance of free space, $\mu(\omega)$ is the magnetic permeability, $\epsilon(\omega)$ is the permittivity, and ω is the frequency. An infrared signal with a frequency matching the absorption spectrum of the MS will be absorbed. To detect events such as forest fires (infrared radiation wavelengths of 2–5 μm ^{25–27}) and the appearance of humans (infrared radiation wavelengths of 9 μm ²⁸), we designed two types of MSs with different absorption spectra (wavelengths of 2–5 μm and 9 μm) via the finite-difference time-domain (FDTD) method. The important geometry parameters are shown in

Table 1 Geometric parameters of the MS with an absorption wavelength of 2–5 μm

Parameters	Description	Size (μm)
a	Spacing between metal antennas	1.13
w	Square side length	0.77
t_1	Metal antenna thickness	0.05
t_2	Si ₃ N ₄ thickness	0.3
t_3	Bottom metal layer thickness	0.05
t_4	Glass substrate thickness	200

Tables 1 and 2. The morphologies of the fabricated MSs were characterized by scanning electron microscopy (SEM), as shown in Fig. 2a, b. Fourier transform infrared spectroscopy (FTIR) was employed to characterize the absorption characteristics of the MSs, which demonstrated exceptional infrared absorptivity ($\geq 85\%$) and excellent frequency selectivity (Fig. 2c, d).

Two-phase microfluidic flow

To realize a reliable switch, it is essential to keep the two-phase microfluidic interface stable and avoid mixing kerosene and the FeCl₃ solution during

switching. We first investigated the impact of channel surface wettability on the two-phase microfluidic flow. Kerosene has a high affinity for glass surfaces, so it can easily form a wetting layer and envelop the FeCl₃ solution. To address this problem, we coated the microchannels with silicone polymer as a hydrophobic layer. As a result, the contact angle of kerosene on the glass surface increased from <5 to 61°, and the contact angle of the FeCl₃ solution increased from 33 to 116° (Fig. 3a). Figure 4b shows stable and unstable kerosene/FeCl₃ two-phase microfluidic flows. Devices with hydrophobic coatings are more likely to remain stable. For unstable microfluidics, boundary residuals²⁹ and

the envelopment of aqueous solutions by oil wetting³⁰ were observed (Fig. 3b). The impacts of the channel width and flow rate on the properties of the two-phase microfluidic flow were also systematically investigated. Our experimental results indicate that a lower fluid velocity and smaller channel width are essential for realizing stable two-phase microfluidic flow (Fig. 3c, d). Additionally, without a hydrophobic coating, the stable two-phase microfluidic flow can only move at a speed of 1000 μm/s, whereas with a hydrophobic coating, the speed can reach 5000 μm/s. The hydrophobic coating allows the two-phase microfluidic flow to remain stable at relatively high velocities in the microchannel. Reliable two-phase microfluidic switches were realized on the basis of this study. This approach is important for the fundamental research and application of two-phase microfluidics.

Table 2 Geometric parameters of the MS with an absorption wavelength of 9 μm

Parameters	Description	Size (μm)
a	Spacing between metal antennas	2.2
w ₁	Cross length	1.83
w ₂	Cross width	1.1
t ₁	Metal antenna thickness	0.05
t ₂	Si ₃ N ₄ thickness	0.3
t ₃	Bottom metal layer thickness	0.05
t ₄	Glass substrate thickness	200

2D material thermal isolation layer

Kerosene in the reservoir absorbs the heat generated from the MS, resulting in volume expansion ΔV, which can be expressed as:

$$\Delta V = \frac{\alpha}{C_p} Q \tag{2}$$

where α is the thermal expansion coefficient of kerosene, C is the heat capacity, ρ is the density of kerosene, and Q

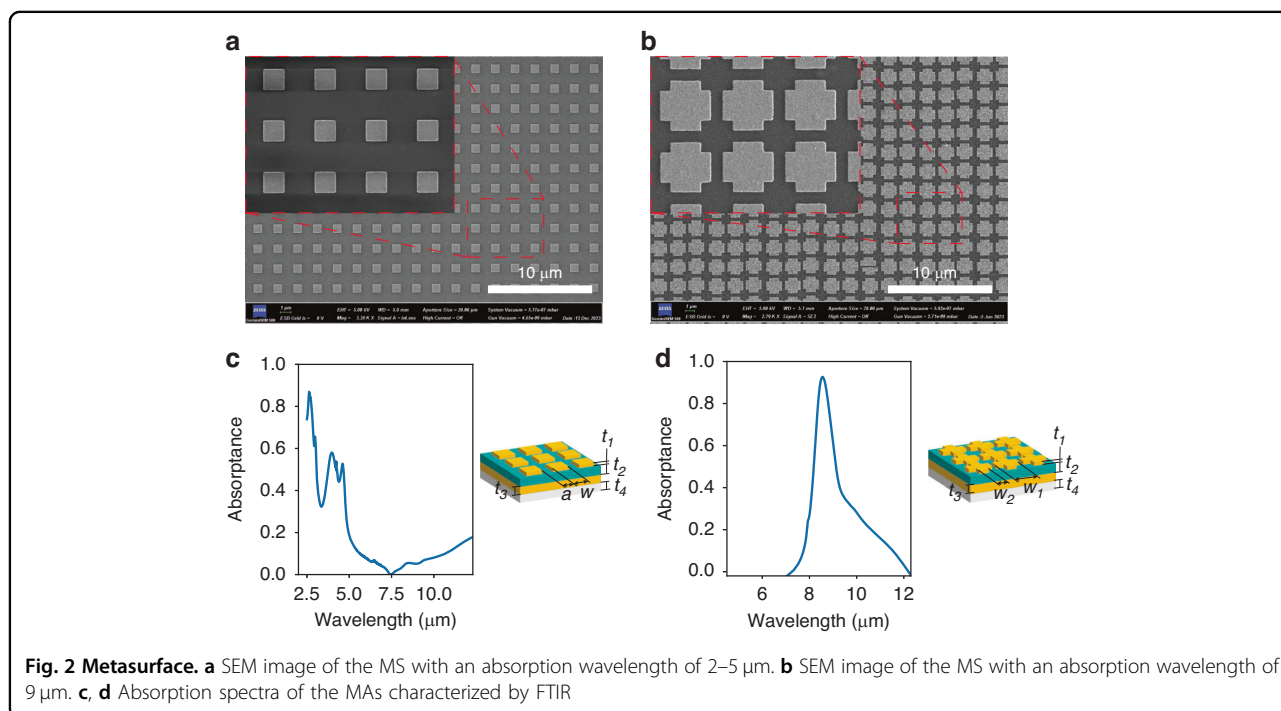
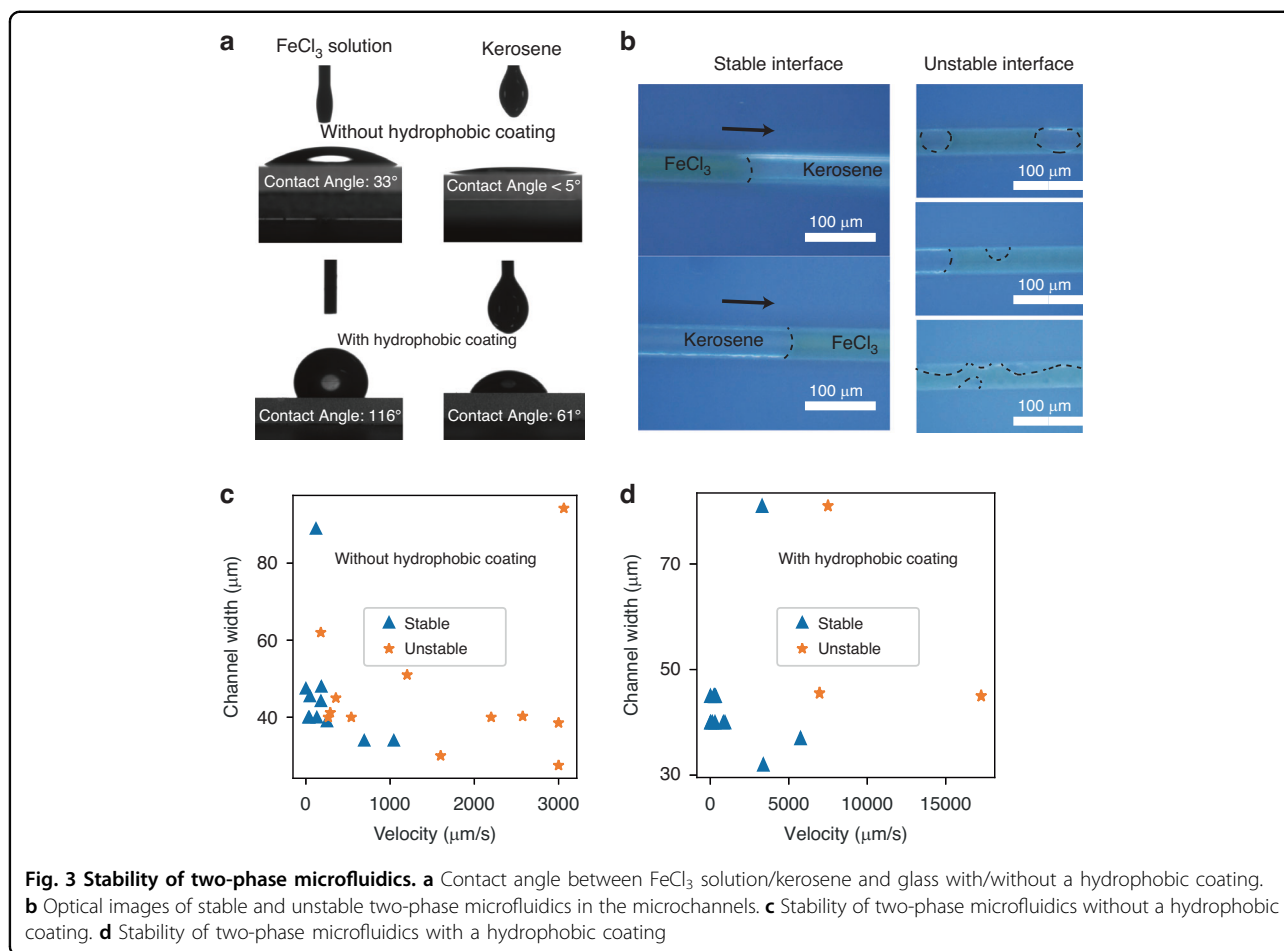


Fig. 2 Metasurface. a SEM image of the MS with an absorption wavelength of 2–5 μm. **b** SEM image of the MS with an absorption wavelength of 9 μm. **c, d** Absorption spectra of the MAs characterized by FTIR



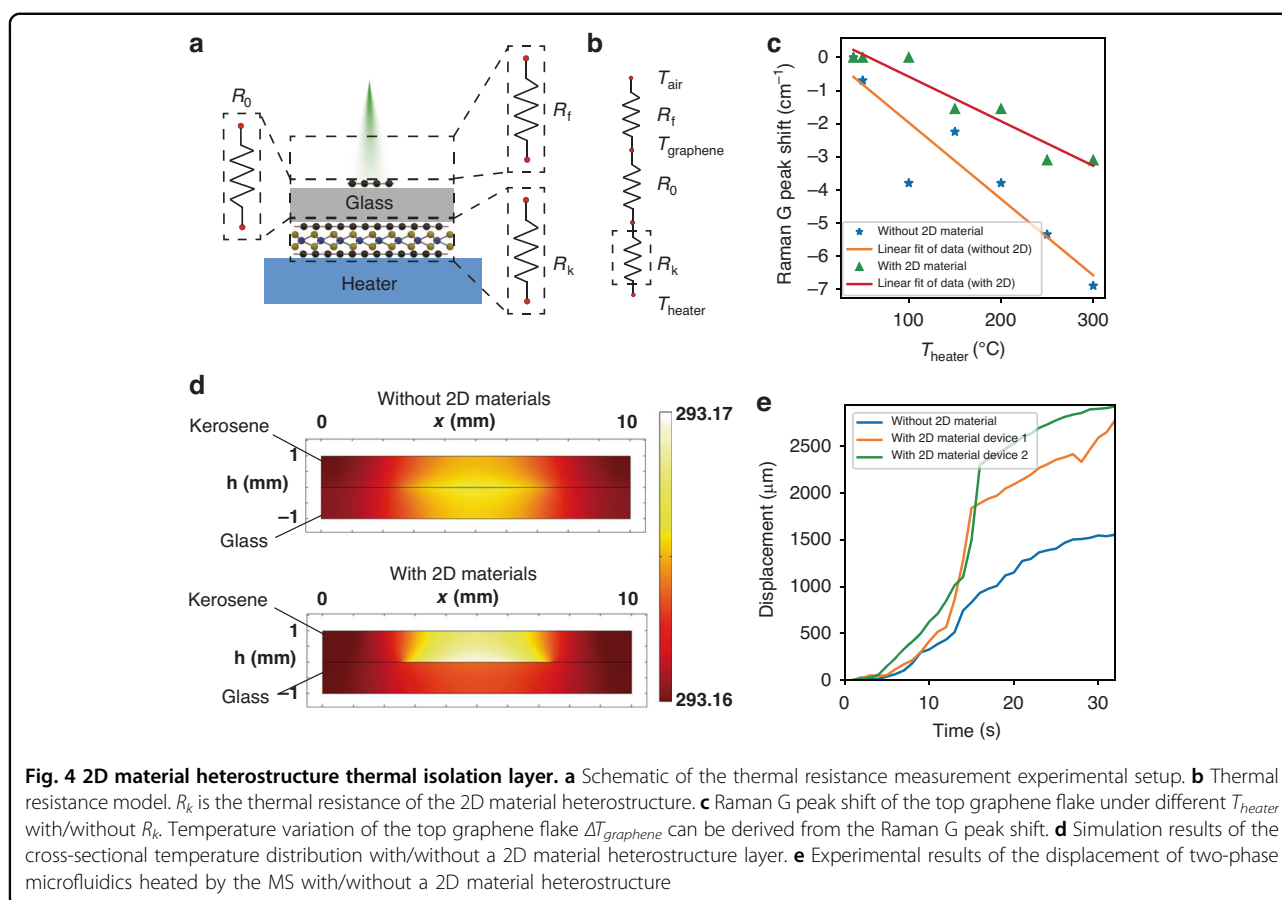
is the heat absorbed by kerosene. Given that the infrared energy from the target is very low, thermal isolation is important for reducing heat dissipation and enhancing device sensitivity. Owing to the low thermal conductivity of kerosene (0.2 W/m · K), immersing the MS in kerosene greatly increases the heat absorbed by kerosene. However, the 200 μm -thick supporting substrate of the MS has a much larger heat capacity than that of the MIM sandwich structure, whose thickness is less than 0.5 μm . As a result, a considerable amount of heat generated will be absorbed by the supporting substrate of the MS instead of kerosene. Therefore, a thermal isolation layer with superb thermal resistance and ultrasmall heat capacity is desired (the thermal isolation layer itself absorbs a negligible amount of heat).

Two-dimensional material heterostructures have extremely high thermal resistance in the vertical direction because the thickness of the monolayer 2D material is smaller than the mean free path of molecules, which results in strong phonon scattering at the interface^{31,32}. The phonon density of states (PDOS) can describe the heat transfer effect at the nanoscale³³. According to

Vaziri et al.³⁴:

$$TBC \propto Trans. \times PDOS\ overlap \times df/dT \quad (3)$$

where TBC is the thermal boundary conductivity (a smaller TBC indicates a stronger thermal isolation capability) and $Trans$ is the mass density mismatch. The $PDOS\ overlap$ is the overlap between the PDOSs of two contacting materials, and df/dT is the derivative of the Bose-Einstein distribution function with respect to temperature. The mass density mismatch between graphene and MoS₂ is 0.448, and the number of modes for the PDOS overlap is 3.9×10^{15} , indicating a low TBC and good thermal isolation properties of the 2D material heterostructure (graphene/MoS₂)³⁴. Additionally, atomically thin 2D material heterostructures have ultrasmall heat capacities. However, previous research focused on the thermal isolation characteristics of mechanically exfoliated micrometer-sized 2D material flakes, which are unsuitable for practical use. The thermal isolation characteristics of large-area CVD 2D material heterostructures remain unknown.



Here, we measured the thermal resistance of a large-area (graphene/MoS₂/graphene) 2D material heterostructure and demonstrated its practical application in MEMS devices for the first time. Graphene and MoS₂ are the most intensively studied 2D materials. Compared with other 2D materials, large-area graphene and MoS₂ films synthesized by CVD have better properties, and the CVD technique for graphene/MoS₂ growth is relatively reliable. In addition, graphene and MoS₂ demonstrate good stability, whereas some 2D materials, such as black phosphorus, are unstable in ambient environments. Therefore, graphene and MoS₂ were chosen for constructing vertical heterostructures. To measure the thermal resistance of the CVD graphene/MoS₂/graphene heterostructure, the thickness of which is less than 2 nm, the heterostructure was transferred to the bottom side of the glass substrate, as shown in Fig. 4a, and a mechanically exfoliated small graphene flake was transferred to the top surface of the glass substrate as a microthermometer. We heated the bottom side of the glass substrate, and the temperature variation of the top graphene flake $\Delta T_{graphene}$ was measured via Raman microscopy as the graphene G peak shifted to $-0.02 \text{ cm}^{-1}/\text{K}$. We prepared samples

without a 2D material heterostructure as the control group. Compared with the control samples, the samples with a heterostructure isolation layer clearly demonstrated a smaller Raman shift (Fig. 4c), indicating a smaller $\Delta T_{graphene}$ and superior thermal isolation characteristics of the CVD graphene/MoS₂/graphene heterostructure. According to our experimental results, the larger-area CVD graphene/MoS₂/graphene heterostructure has an ultralarge vertical direction thermal resistance of 4.2 K/W, and the effective thermal conductivity is $3.5 \times 10^{-6} \text{ W}/(\text{m}\cdot\text{K})$. The temperature distributions of the MS (with/without the graphene/MoS₂/graphene heterostructure) in the infrared switch and surrounding kerosene after 20 s of infrared radiation were simulated via COMSOL (Fig. 4d). The graphene/MoS₂/graphene heterostructure significantly reduces the heat flow from the MIM to the glass substrate. As a result, the kerosene above the MIM has a higher temperature (Fig. 4d). We then experimentally investigated the displacement of two-phase microfluidic flows heated by different MSs (infrared power intensity of $32 \mu\text{W}/\text{mm}^2$). With the graphene/MoS₂/graphene heterostructure, the displacement of the microfluidic flow reached $\sim 3000 \mu\text{m}$ after 30 s of infrared radiation, whereas the value greatly decreased to $\sim 1500 \mu\text{m}$ without the

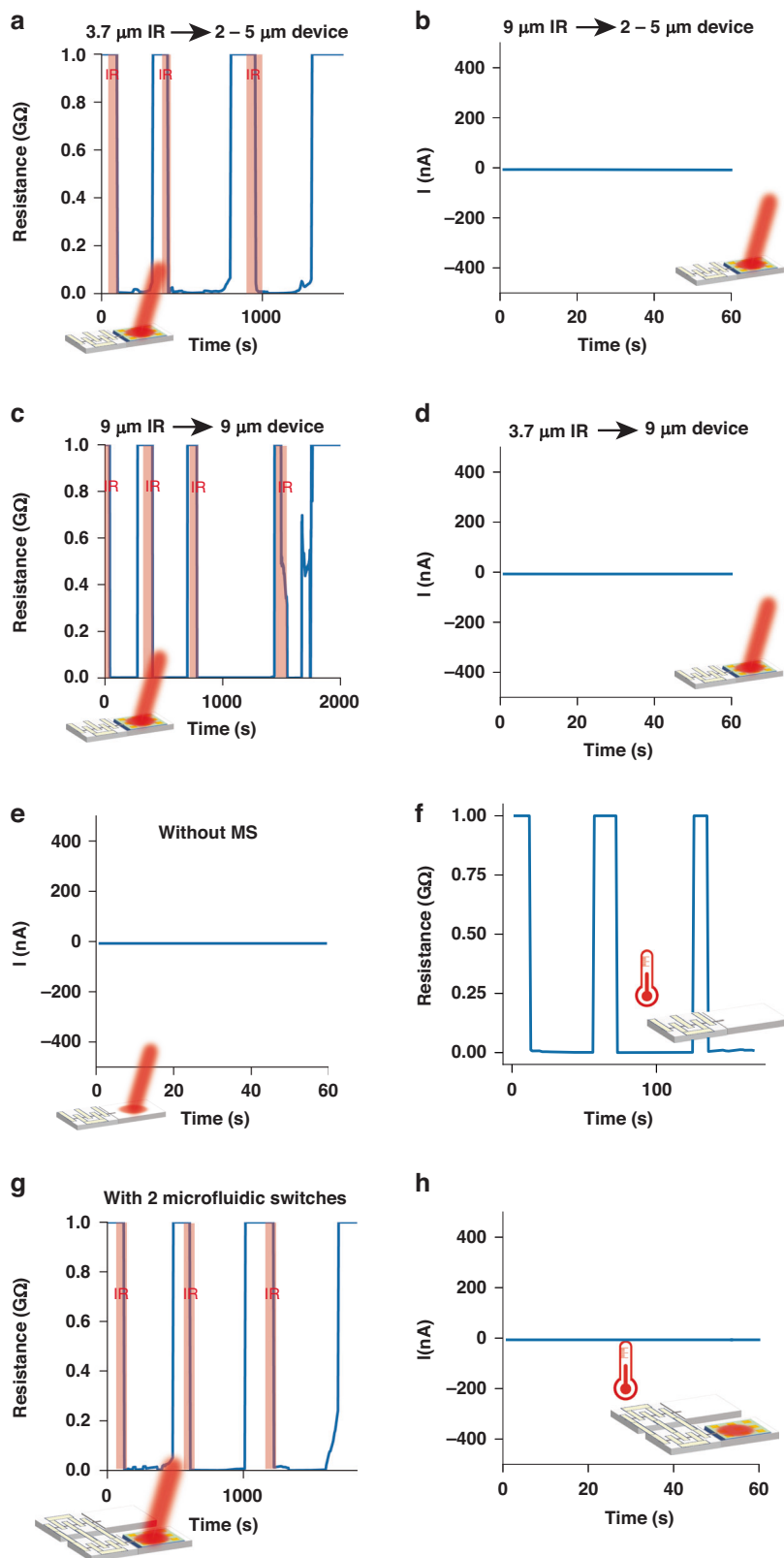


Fig. 5 (See legend on next page.)

(see figure on previous page)

Fig. 5 Sensing performance of the infrared switch. **a** Single microfluidic switch with the MS (absorption wavelength of 2–5 μm) under 3.7 μm infrared irradiation. **b** Single microfluidic switch with the MS (absorption wavelength of 2–5 μm) under 9 μm infrared irradiation. **c** Single microfluidic switch with the MS (absorption wavelength of 9 μm) under 9 μm infrared irradiation. **d** Single microfluidic switch with the MS (absorption wavelength of 9 μm) under 3.7 μm infrared irradiation. **e** Single microfluidic switch without the MS under infrared irradiation. **f** Single microfluidic switch under ambient temperature variation. **g** Infrared switch with a pair of microfluidic flows under infrared irradiation. **h** Infrared switch with a pair of two-phase microfluidics under ambient temperature variation

graphene/MoS₂/graphene heterostructure (Fig. 4e). Therefore, the 2D material heterostructure thermal isolation layer significantly enhances the device sensitivity.

Sensing performance of the infrared switch

Figure 5a, b displays the characteristics of a two-phase microfluidic switch integrated with the MS whose absorption wavelength is 2–5 μm . Under 3.7 μm wavelength infrared irradiation, the microfluidic switch was turned on within ~ 15 s and slowly switched to the ‘off’ state as the infrared source was turned off. Figure 5a shows the excellent repeatability of our microfluidic switch. Notably, the upper limit of the digital multimeter is $10^9 \Omega$; thus, the actual ‘off’ state resistance of our microfluidic switch exceeds $10^9 \Omega$, and the on/off ratio can reach 10^6 . The same device showed no response to 9 μm wavelength infrared radiation (Fig. 5b), demonstrating excellent frequency selectivity. Figure 5c, d illustrates the characteristics of a two-phase microfluidic switch integrated with the MS whose absorption wavelength is 9 μm ; it can only be activated by 9 μm infrared irradiation and showed no response to 3.7 μm infrared irradiation. The sensitivity of the switch is 257 $\mu\text{m}/\text{mW}$ (1 mW infrared energy results in 257 μm displacement of the two-phase flow). In the control group, a two-phase microfluidic switch without the MS showed no response to (3.7 μm or 9 μm) infrared irradiation (Fig. 5e). Additionally, a single two-phase microfluidic switch was sensitive to environmental temperature changes (it turned on as the temperature increased to ~ 0.5 $^\circ\text{C}$, Fig. 5f).

To eliminate the impact of environmental temperature variation, we fabricated a device with a pair of symmetric two-phase microfluidic switches, and only one microfluidic switch was integrated with the MS (absorption wavelength of 2–5 μm) in the reservoir. As demonstrated in Fig. 5g, h, the infrared switch was sensitive to (3.7 μm wavelength) infrared irradiation. It turned on within 20 s and maintained the ‘on’ state for ~ 300 s after the infrared source was turned off, demonstrating excellent switching performance and self-holding ability (Fig. 5g). Figure 5h shows that the infrared switch remained in the ‘off’ state without infrared irradiation as the ambient temperature changed (~ 0.5 $^\circ\text{C}$), indicating that spurious triggering

resulting from environmental temperature changes can be avoided.

Near-zero-standby-power WSNs

We realized near-zero-standby-power WSNs with visual/auditory functions by integrating the infrared switch, sensors (CCD/MEMS microphone), and wireless communication module (Fig. 6a). In the absence of infrared signals, the infrared switch was in the ‘off’ state. The WSNs were completely turned off and demonstrated near-zero standby power, as shown in Fig. 6b, d. As the infrared switch was illuminated by the target infrared signal, it turned on and activated the sensors integrated in the WSNs. In WSNs with visual function, the CCD captures an image (the logo of Tsinghua University) and transfers it to a remote terminal via a wireless communication module. The image received is shown in the inset of Fig. 6b. In WSNs with auditory function, a MEMS microphone was activated and started to record environmental sounds and transmit the information to a remote terminal. Figure 6c shows the audio waveform received as the tester said “nanotechnology”, “nanofabrication”, and “metamaterials”. Therefore, unattended WSNs with near-zero standby power were realized.

Conclusion

In summary, we realized zero-power infrared switches by integrating an MS and two-phase microfluidic switches. The MS can recognize the infrared signals from the target and convert them into heat, which turns on the two-phase microfluidic switch. The impacts of the channel width, flow rate, and surface wettability on the properties of two-phase microfluidics were systematically investigated, and reliable two-phase microfluidic switches were realized on the basis of this fundamental study. The graphene/MoS₂/graphene heterostructure has exceptional thermal isolation capability because strong phonon scattering reduces the heat flow from the MS to the substrate and significantly increases the device sensitivity. We realized near-zero-standby-power WSNs by integrating the infrared switches with a CCD/MEMS microphone and a wireless communication module. This work not only provides an approach for greatly lengthening the lifespan of WSNs but also may stimulate fundamental research and the application of two-phase microfluidics and nanoscale thermal isolation.

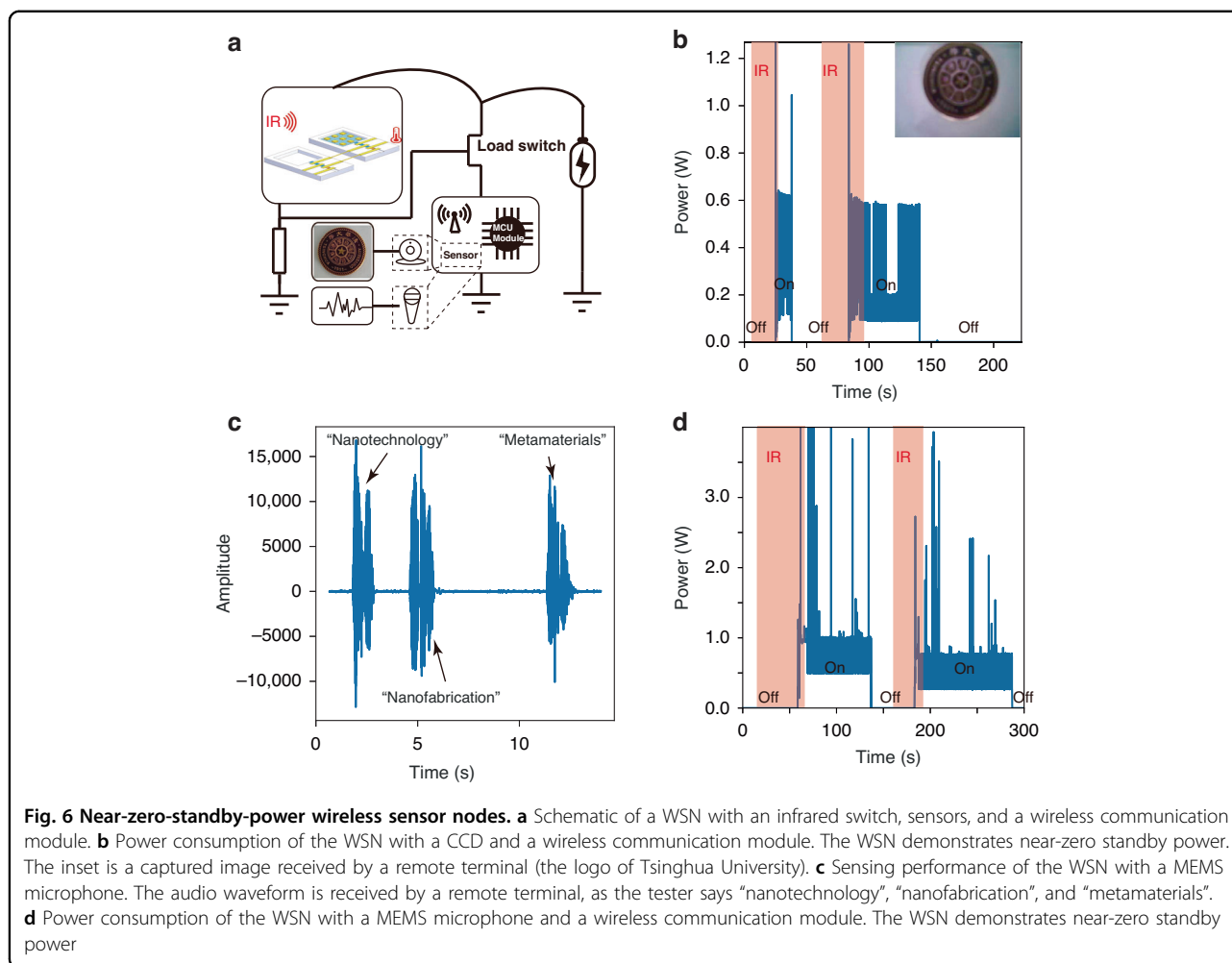


Fig. 6 Near-zero-standby-power wireless sensor nodes. **a** Schematic of a WSN with an infrared switch, sensors, and a wireless communication module. **b** Power consumption of the WSN with a CCD and a wireless communication module. The WSN demonstrates near-zero standby power. The inset is a captured image received by a remote terminal (the logo of Tsinghua University). **c** Sensing performance of the WSN with a MEMS microphone. The audio waveform is received by a remote terminal, as the tester says "nanotechnology", "nanofabrication", and "metamaterials". **d** Power consumption of the WSN with a MEMS microphone and a wireless communication module. The WSN demonstrates near-zero standby power

Acknowledgements

This work was supported by the National Natural Science Foundation of China (52322512, 51775306).

Author contributions

P.L. conceived the experiments. Z.Z. and Y.Z. fabricated the devices and performed the measurements. P.L., Z.Z., Y.Z. analyzed the results. P.L. and Z.Z. cowrote the manuscript. All authors discussed the results and commented on the manuscript.

Conflict of interest

The authors declare no competing interests.

Received: 27 February 2024 Revised: 10 June 2024 Accepted: 2 July 2024

Published online: 02 September 2024

References

- Masako, T. An industrial and applied review of new MEMS devices features. *Microelectron. Eng.* **84**, 1341–1344 (2007).
- Nuzzo, F. D. et al. Structural health monitoring system with narrowband IoT and MEMS sensors. *IEEE Sensors J.* **21**, 16371–16380 (2021).
- Dong, S. et al. MEMS-based smart gas metering for Internet of Things. *IEEE Internet Things J.* **4**, 1296–1303 (2017).
- Tokogon, C. A. et al. Structural health monitoring framework based on Internet of Things: a survey. *IEEE Internet Things J.* **4**, 619–635 (2017).
- Roundy, S. et al. Power sources for wireless sensor networks. In *Wireless Sensor Networks: First European Workshop, EWSN 2004. Proceedings* vol 1, pp 1–17 (Springer, Berlin, Germany, 2004).
- Saldamli, G. et al. Wildfire detection using wireless mesh network. In *2019 IEEE FMEC*, 229–234 (IEEE, 2019).
- Shu, L. et al. A survey on gas leakage source detection and boundary tracking with wireless sensor networks. *IEEE Access* **4**, 1700–1715 (2016).
- Ahmed, M. et al. Broadband zero-power wakeup MEMS device for energy-efficient sensor nodes. *Micromachines* **13**, 407 (2022).
- Han, Y. et al. Low-G triggered acceleration switch for near-zero power wakeup application. *Micromachines* **13**, 1333 (2022).
- Hu, D. et al. Strategies to achieve high performance piezoelectric nanogenerators. *Nano Energy* **55**, 288–304 (2019).
- Li, P. et al. A self-powered 2D-material sensor unit driven by a SnSe piezoelectric nanogenerator. *J. Mater. Chem. A* **9**, 4716–4723 (2021).
- Lu, S. et al. Simultaneous energy harvesting and signal sensing from a single triboelectric nanogenerator for intelligent self-powered wireless sensing systems. *Nano Energy* **75**, 104813 (2020).
- Mangaiyarkarasi, P. & Lakshmi, P. Design of piezoelectric energy harvester using intelligent optimization techniques. In *2018 IEEE PEDES*, 1–6 (IEEE, 2018).
- Panda, S. et al. Piezoelectric energy harvesting systems for biomedical applications. *Nano Energy* **100**, 107514 (2022).
- Jiang, J. A. et al. A novel sensor placement strategy for an IoT-based power grid monitoring system. *IEEE Internet Things J.* **7**, 7773–7782 (2020).

16. Merlin, C. J. & Heinzelman, W. B. Schedule adaptation of low-power-listening protocols for wireless sensor networks. *IEEE Trans. Mob. Comput.* **9**, 672–685 (2009).
17. Dudko, U. & Overmeyer, L. Optical wake-up from power-off state for autonomous sensor nodes. *IEEE Sensors J.* **21**, 3225–3232 (2020).
18. Pinrod, V. et al. Zero-power sensors with near-zero-power wakeup switches for reliable sensor platforms. In *2017 IEEE MEMS*, 1236–1239 (IEEE, 2017).
19. Truong, S. K. M. et al. Demonstration of 155.1 μ W wake-up gas sensor node toward 8 month lifetime. In *2020 IEEE MEMS*, 622–625 (IEEE, 2020).
20. Qian, Z. et al. Zero-power infrared digitizers based on plasmonically enhanced micromechanical photoswitches. *Nat. Nanotech.* **12**, 969–973 (2017).
21. Dao, T. D. et al. Infrared perfect absorbers fabricated by colloidal mask etching of Al–Al₂O₃–Al trilayers. *ACS Photonics* **2**, 964–970 (2015).
22. Felbacq, D. & Bouchitté, G. Left-handed media and homogenization of photonic crystals. *Opt. Lett.* **30**, 1189 (2005).
23. Guo, W. L. et al. Ultra-broadband infrared metasurface absorber: reply. *Opt. Express* **27**, 5351 (2019).
24. Liu, N. et al. Infrared perfect absorber and its application as plasmonic sensor. *Nano Lett.* **10**, 2342 (2010).
25. Aranda, J. M. et al. Forest fire studies by medium infrared and thermal infrared thermography. *Thermosense XXIII*. **4360**, 161–168 (2001).
26. Aranda, J. M. et al. Measurement of physical parameters of forest fires by infrared imaging methods. *WIT Trans. Ecol. Environ* **119**, 111–120 (2008).
27. Melendez, J. et al. Measurement of forest fire parameters with multi-spectral imaging in the medium infrared. *QIRT* **3**, 183–199 (2006).
28. Hardy, J. D. & Muschenheim, C. Radiation of heat from the human body. V. The transmission of infra-red radiation through skin. *J. Clin. Investig.* **15**, 1–9 (1936).
29. Han, Y. & Shikazono, N. Measurement of liquid film thickness in micro square channel. *Int. J. Multiphas. Flow* **35**, 896–903 (2009).
30. Foroughi, H. et al. Immiscible displacement of oil by water in a microchannel: asymmetric flow behavior and nonlinear stability analysis of core-annular flow. *Phys. Rev. E* **85**, 026309 (2012).
31. Ding, Z. W. et al. Interfacial thermal conductance in graphene/MoS₂ heterostructures. *Carbon* **96**, 888–896 (2016).
32. Wu, S. et al. Interfacial thermal conductance across graphene/MoS₂ van der Waals heterostructures. *Energies* **13**, 5851 (2020).
33. Zhu, J. et al. Molecular dynamics study of the thermal transport properties in the graphene/C₃N multilayer in-plane heterostructures. *Heat Transfer Res.* **55**, (2024).
34. Vaziri, S. et al. Ultrahigh thermal isolation across heterogeneously layered two-dimensional materials. *Sci. Adv.* **5**, eaax1325 (2019).